Customized OCT images compression scheme with deep neural network

PENGFEI GUO[1,4] DAWEI LI,[2,4] AND XINGDE LI[2,3*]

[1]*Department of Computer Science, Johns Hopkins University, Baltimore, MD 21218, USA,*
[2]*Department of Biomedical Engineering, Johns Hopkins University, Baltimore, MD 21205, USA,*
[3]*Department of Electrical and Computer Engineering, Johns Hopkins University, Baltimore, MD 21218,*
[4]*Equal contribution*
*xingde@jhu.edu

Abstract: We customize an end-to-end image compression framework for retina OCT images based on deep convolutional neural networks (CNNs). The customized compression scheme consists of three parts: data Preprocessing, compression CNNs, and reconstruction CNNs. Data preprocessing module reduces the speckle noise of the OCT images and the segments out the region of interest. We added customized skip connections between the compression CNNs and the reconstruction CNNs to reserve the detail information and trained the two nets together with the semantic segmented image patches from data preprocessing module. To train the two networks sensitive to both low frequency information and high frequency information, we adopted an objective function with two parts: A PatchGAN discriminator to judge the high frequency information and a differentiable MS-SSIM penalty to evaluate the low frequency information. The proposed framework was trained and evaluated on a publicly available OCT dataset. The evaluation showed above 99% similarity in terms of multi-scale structural similarity (MS-SSIM) when the compression ratio is as high as 40. Furthermore, the reconstructed images of compression ratio 80 from the proposed framework even have better quality than that of compression ratio 20 from JPEG by visual comparison. The testing result outperforms JPEG in term of both of MS-SSIM and visualization, which is more obvious as the increase of compression ratio. Our preliminary result indicates the huge potential of deep neural networks on customized medical image compression.

1.Introduction

Remote disease diagnosis and monitoring, such as Optical Coherence Tomography (OCT) based Age-related Macular Degeneration (AMD) detection and management, demands efficiently data transferring and storage. A high efficient medical images compression framework would be extremely beneficial to such remote diagnosis and monitoring systems by providing high-fidelity images for diagnosis with extremely high compression rate. Specifically, for ophthalmic OCT images, it is necessary to preserve the detail of retina layers and fine structural information from the noisy background [3].

The general compression format, such as JPEG, becomes suboptimal as the increase of compression rate [3] and customized compression methods, such as compressive sensing (CS), provides an alternative way [4]. While the CS-based compression algorithm suffers from expensive computation memory and limited improvement of compression performance [5]. Currently, Convolutional neural networks (CNNs) provides a new customization approach for image compression [1, 6-8]. However, present works show difficulty to preserve the high resolution structural information for remote diagnosis, especially at a high compression ratio.

In this paper, we customized compression framework based on a deep neural network to provide high fidelity image up to 80:1 compression ratio. The proposed scheme works in two stages: First, distinguishing diagnostic features of interest from noisy background by sematic segmentation [2, 9]; then, compressing the original images with CNNs and providing a reconstruction CNNs to interpret the compressed files. This paper will first present the working

scheme and how to train the CNNs for compression and reconstruction in detail. Then, the paper will demonstrate the performance of the proposed compression method which includes quantitative and qualitative comparison between proposed method and JPEG. In the end, we will discuss the novelty and prospect of the method.

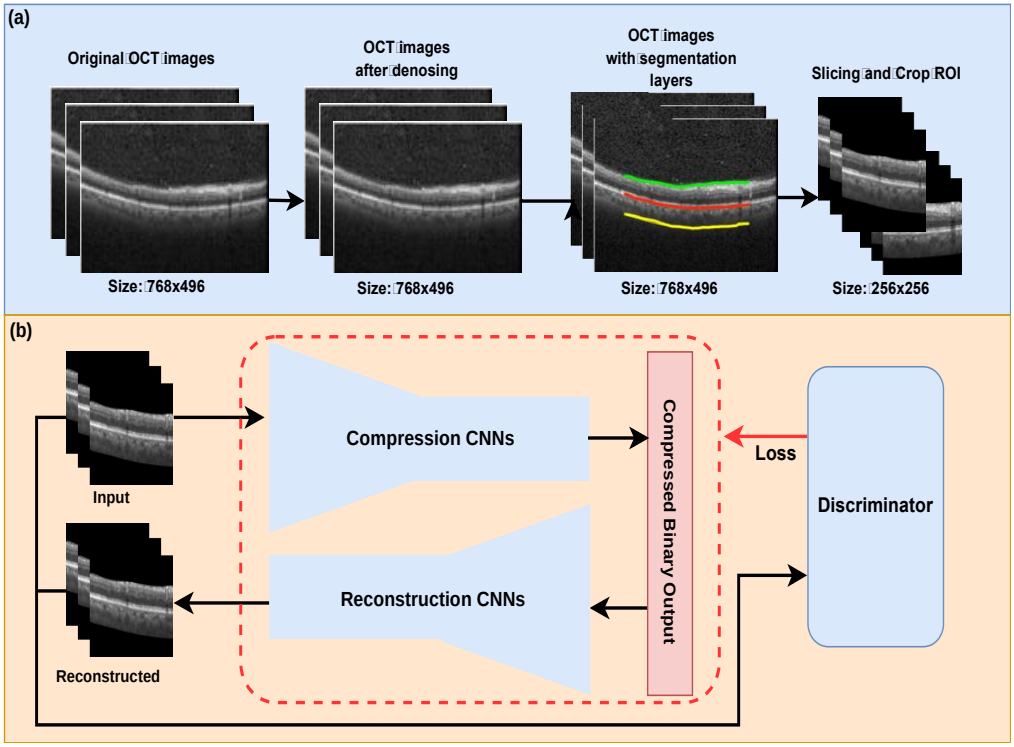

Fig.1 (a) Schematic of data preprocessing procedure. There were three layers results from segmentation: 1. ILM (green line): Inner Limiting membrane line; 2. BM (red line): Bruch's Membrane; 3. LBM (yellow line): Lower boundary corresponding to BM. (b) Schematic of compression workflow, which essentially is a conditional GANs model that contains a Generator, including compression CNNs and reconstruction CNNs, and a discriminator (train phrase only). The compressed binary output came from last layer of compression CNNs after a quantization procedure.

2. Method

The customized compression framework consists of three parts: data preprocessing module (see Fig. 1(a)), CNNs based image compression module and CNNs based reconstruction module (see Fig. 1(b)). The compressed file is output of the compression CNNs which consists of a bitstream that perceives image information and the reconstruction CNNs serves as a dictionary to interpret the bitstream to high resolution images. First, we reduce the speckle noise of the OCT images and segment out the region of interest related to disease diagnosis, for both training and testing phase. Then, we train the compression and reconstruction CNNs together with an objective function combined by a PatchGAN module and a differentiable MS-SSIM penalty module. The training is processed in an adversarial way.

2.1 Date Preprocessing

2.1.1 Denoising and Segmentation

As OCT imaging is based on low-coherence interferometry, it suffers from speckle noise. Speckle noise not only degrades OCT image quality and makes it difficult to identify the small detailed structures but also leads to the fake guidance when we train the compression and reconstruction CNNs. To efficiently compress the OCT images and keep high fidelity structural information, we reduce the sparkle noise in the OCT images at the first step [9-11] (see Fig. 1(a)). To further increase the compression rate, we segment out the region of interest for disease diagnosis. The semantic segmentation approach is based on well-established CNNs models [12-14].

To run the image compression processing efficiently and avoid potential memory overflow, each original image with size of 496 × 768 pixels was cropped out along upper and lower boundaries (see green and yellow line in Fig. 1. (a)) and padded to rectangular images, resulting in a final image size of 256 × 512 pixels before compression [2]. In order to fit in compression CNNs, each rectangular image was evenly divided into two square images with size of 256 × 256 pixels (see Fig.1(a)). The above data preparation procedure resulted a dataset consisting of 980 train images, 240 validation and test images (180 validation images and 60 test images). The all train images were then augmented by horizontal flipping and random cropping before entering the compression CNNs during the train phase to prevent potential overfitting problems [1, 13]. We trained the compression CNNs and reconstruction CNNs with 980 square OCT images (ground truth). For the rest of images, 180 images served as validation data set for tuning hyper-parameters. We tested the trained compression framework with 60 images and made final quality measurement. Each train, validation, and test dataset were randomly selected without any overlap.

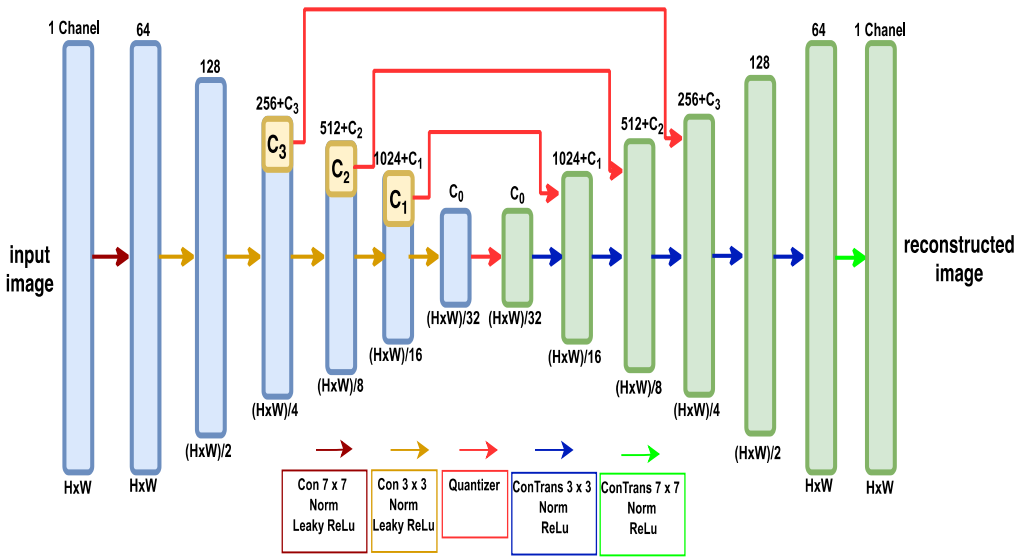

Fig. 2. Schematic of a generation in conditional GANs model, which contains compression CNNs (blue blocks in left side) and reconstruction CNNs (green blocks in left side). Leaky Rectified Linear Unit (Leaky ReLu) and Rectified Linear Unit (ReLu) induced nonlinearity for efficient training [1]. Convolution layers with stride 2 reduce feature maps by a factor of 2 along each dimension [2]. The red arrows indicated feature maps from compression CNNs to reconstruction CNNs via a quantizer.

2.2 Architecture of Networks

2.2.1 Compression CNNs and Reconstruction CNNs

The schematic of compression and reconstruction CNNs with quantization procedure is shown in Fig. 2. The compression CNNs contract the dimension of input images layer by layer, and the reconstruction CNNs expand the dimension in a symmetrical way. In detail, six layers in each CNNs learn the contextual feature information and hierarchically contract the dimension of original input images. A quantizer lays at the bottom of the compression layer to generate a bitstream as the output. Three skip connections concatenate two CNNs and feed the image information on different scale into the quantizer. (the three red arrows pass through the quantizer from left to right quantizer in Fig. 2). The skip connections preserve high resolution information of compression CNNs and transfer it to corresponding reconstruction layers. The dimension of each input for the compression CNNs is 256 × 256 pixels. The input is first augmented by randomly flipping and then fed into the compression layers. The first layer applies convolution with 64 kernels (size of 7 × 7 pixels) to generate a (256 × 256) × 64 feature maps, normalization, and a Leaky ReLu activation function with slope 0.2 to prepare the down-sampling process. Five more layers with similar modules follow with a down sampling rate of 2 × 2. At the bottom of compression CNNs, contracted feature maps with dimension of ($\frac{\mathrm{H}}{32} \times \frac{\mathrm{W}}{32}$) $\times C_0$ (where C_0 is the number of channels; H×W is the spatial dimension of input images) are transited through quantizer to the reconstruction net. The reconstruction CNNs symmetrically reverse the process in compression CNNs side but we replaced Leaky ReLu activation functions by ReLu activation functions to achieve better reconstruction quality [1]. In order to enhance the resolution of up-sampling process, similarly in U-Net, three skip connections concatenate a part of output feature maps of third, fourth, and fifth layer of compression CNNs and reconstruction CNNs through quantizer [15-19]. We use C_1, C_2, and C_3 to respectively control the number of channels in each skip connections. The output of reconstruction CNNs have exact same dimension of the input.

2.2.2 Multi-scale Quantization and Compressed Output

The red arrows in Fig. 2 indicate the quantizer which quantized the feature maps from different compression layers to generate a bitstream as the output. The output consists of two parts: the majority is from the last compression layer; The rest is from the 3 skip connections that partially contain the feature maps from "upper" layers. We combine two parts together, quantize them as output.

We adopt a scalar variant design in quantization process [7], in which the figure maps are quantized to L levels and then encoded to a bitstream [20]. We control the compression ratio with two parameters: the spatial dimension of the input feature maps of the quantizer and the quantization level L. compression ratio can be expresses as below:

$$Compression\ Ratio\ (CR) = \frac{H_{input} \cdot W_{input} \cdot S}{\sum_{i=0}^{n} H_i \cdot W_i \cdot C_i \cdot \log_2 L} \tag{1}$$

Where n is the number of connections passing through quantizer between compression and reconstruction nets; $(H_i \cdot W_i \cdot C_i)$ is the spatial dimension of feature maps in each connection; S is the bit depth of input the image. In our work, the dimensions of input figure maps are $(8 \times 8 \times \mathrm{C}_0)$, $(16 \times 16 \times \mathrm{C}_1)$, $(32 \times 32 \times \mathrm{C}_2)$ and $(64 \times 64 \times C_3)$; the quantitation level is 7. By changing the number of channels in feature maps, we can achieve compression ratio from 10 to 80.

2.3 Training

2.3.1 Objective function and optimization

In train phase, compression CNNs and reconstruction CNNs are trained together as the generator of conditional GANs [21]. Our objective function consists of two parts: one is the patched decoder as the discriminator of conditional GANs to identify the difference between generated image and original input in an adversarial way.; another is a penalty to evaluate the difference between input and output on different scale in terms of Multi-Scale Structural Similarity (MS-SSIM). A single loss of GANs cannot accurately capture both of low-frequency and high-frequency structures. PatchGAN discriminator is introduced to model high-frequency structures. An additional most-likelihood loss, such as L1, L2, and MS-SSIM loss terms, forces generator to model low-frequency information more efficiently [21]. In our case, we find differentiable MS-SSIM loss results in less blurring of output compared with L1 and L2 norm. The whole objective function is defined as below:

$$L_G = \arg min_G \, max_D L_{cGAN}(G, D) + \lambda L_{MS-SSIM}(G) \tag{2}$$

Where G consists of the compression CNNs and reconstruction CNNs. D indicates the PatchGAN to minimize this objective in adversarial way. Where λ is the weight of MS-SSIM loss. A large weight is selected to exactly reconstruct original input image ($\lambda = 100$ in our case). Specifically, the loos of PatchGAN discriminator can be expressed as blow [21]:

$$L_{cGAN}(G, D) = \mathbb{E}_{x,y}[\log D(x, y)] + \mathbb{E}_{x,z}[\log(1 - D(x, G(x, z))]. \tag{3}$$

Where x is observed input images, y is reconstructed images, and z is random noise that is optional in our model. The criterion of PatchGAN discriminator is to identify whether each N × N patch of the input image is real or not, where N × N patch refers to the receptive field. In our case, we adopt a PatchGAN discriminator architecture with 70 × 70 patch, which consists of four Convolution layers. In each layer, the input feature maps are sequentially applied convolution with (4 × 4 pixels) filters with stride size of 2, instance normalization, and a Leaky ReLu activation function with slope 0.2. After the last layer, the output feature maps are mapped to one-channel output followed by a Sigmoid function which meant the discriminator averaged all responses of each patches to give final output of D by convolutionally across the whole input images [21-23]. During the optimization procedure, we use the Adam optimizer to minimize loss function with $\beta = (0.5, 0.999)$ with a learning rate decay strategy [23, 24].

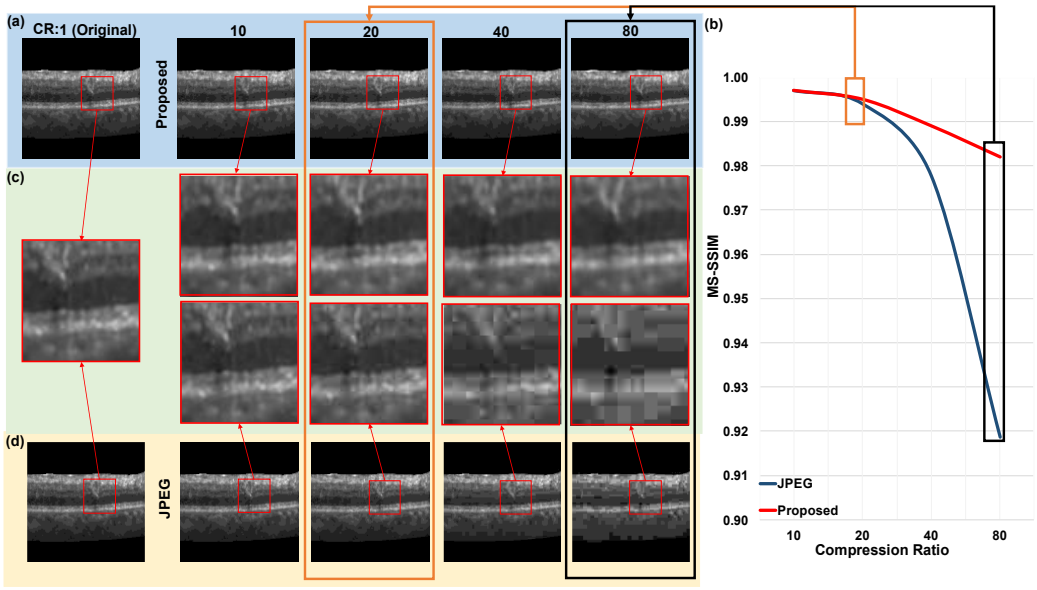

Fig. 3 (a) Visual comparison between original image and proposed compression method at compression ratios 80, 40, 20, 10. (b) Quantitative comparison between proposed compression method and JPEG by CR-Curve. (c) Zoomed-in visual comparison of retina with diagnostic content (we zoom in 8× over all compression ratios). (d) Visual comparison between original image and JPEG at compression ratios 80, 40, 20, 10.

3. Result

In order to measure the quantitative performance of our architectures, we combine MS-SSIM and human visual system which is more sensitive to certain types of distortions than others [25, 26]. MS-SSIM gives a score between 0 and 1. The higher values imply a closer match between the test and reference images. MS-SSIM is defined by below equation:

$$MS-SSIM(x,y) = [l_m(x,y)]^{\alpha_M} \cdot \prod_{j=1}^{M} [c_j(x,y)]^{\beta_j} [s_j(x,y)]^{\gamma_j} \quad (4)$$

Where α_M, β_j, and γ_j are used to ad- just the relative importance of different components[22, 25].

3.1 Comparison with JPEG

We compared the proposed approach with JPEG under a set of compression ratio values (10, 20, 40, and 80, see Fig. 3) [27]. By controlling quantization levels of quantizer and the dimension of latent feature maps from compression CNNs, we trained a set of models at each compression ratio values. Then we tested the trained model on same test dataset. Both the proposed approach (Fig. 3 (a)(c)) and JPEG (Fig. 3 (d)) achieved high similarity index in terms of MS-SSIM at low compression rates (CR < 20) in term of MS-SSIM (Fig. 3(b)). But, the proposed method can constantly keep high similarity index and far outperformed at high compression ratios.

When visualizing the two approaches, the proposed approach preserved perceivably exactly diagnostic content from original images. The outputs of proposed models were more pleasant

to look by human eyes: diagnostic structures like limiting membrane line (ILM) and Bruch's Membrane (BM) were preserved well even the high compression ratio is as high as 80 (see the black rectangle area in Fig. 3 and related zoom-in image). In contrast, JPEG format was suboptimal under the same compression ratio: local structures information degraded severely in terms of obvious block artifacts and blurred high resolution structures. Actually, even at low compression ratios, (at compression ratio 20, see orange rectangle area in Fig. 3), we could easily visualize block artifacts in the JPEG-compressed images— it could cheat the evaluation index, but not human eyes. In contrary, the proposed compression images showed highly visual consistence over all compression ratios.

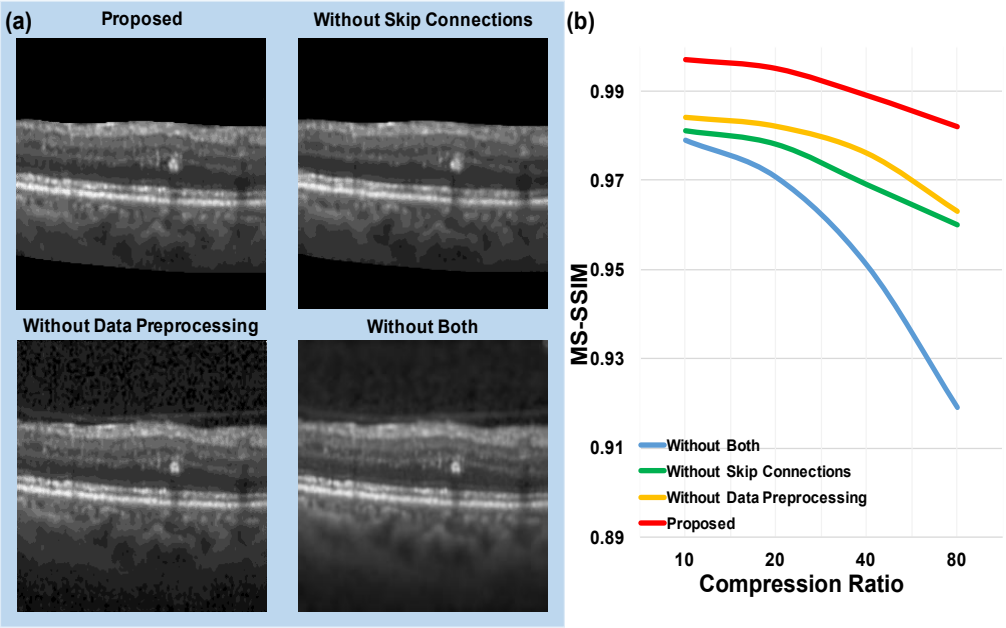

Fig. 4 (a) Visual comparison of reconstructed images between four models at compression ratios 40. (b) Quantitative comparison between proposed method, the method without data preprocessing, the method without skip connections, and the method without both by CR curve.

4. Discussion

In this paper, we customized an OCT image compression framework which can preserve diagnostic features at high compression ratio (as high as 80) with deep neural networks. It outperformed the general compression format JPEG both in similarity index and visual examination. The proposed framework demonstrated superb performance mainly due to three reasons: (1) deep neural networks efficiently compress and reconstruct the image with high fidelity for both low and high frequency information by introducing adversarial PatchGAN discriminator and MS-SSIM penalty in objective function [28, 29]; (2) spackle noise reduction and segmenting out region of interest (ROI) make model focus on specific structural information [30]; (3) customized skip connections enhance the reconstruction resolution by preserving diagnostic information at different scales [31].

Fig. 4 shows the effect of data preprocessing and skip connections clearly in which the results are from the compression and reconstruction CNNs (1) with both data preprocessing and skip connection, (2) only with data preprocessing, (3) only with skip connection and (4) without both. We trained the models with the same hyper-parameters and reconstructed images at same compression ratios. Fig. 4(a) shows the visual comparison. Without denoising and segmenting out ROI, the model was "fouled" by the spackle noise and tried to remember it. As a result, it

degraded the compressed image. Without skip connections, it was more difficult to preserve the high-resolution information and the compressed image was blurred. Without both preprocessing and skip connections, the compressed image was far more suboptimal. Fig. 4(b) shows the quantitative comparison. Data preprocessing and skip connections resulted in obvious distortion reduction performance in terms of MS-SSIM.

Due to these three factors, our model results in comparable performance to the latest published general image compression methods based on deep learning, in which the networks have more complex architectures and are trained with more abundant dataset [8, 27, 32-34]. Furthermore, our computational efficiency of proposed frameworks is also notable. Both compression and reconstruction of an image with size of 512 × 256 pixels only takes about 0.04 s on a Windows computer with the acceleration of a 11 GB memory GPU and PyTorch implementation.

Funding

National Institutes of Health (R01HL121788, R01CA200399), and the Wallace H. Coulter Foundation.

Disclosures

The authors declare that there are no conflicts of interest related to this article. The code will be available by emailing request to jhu.bme.bit@gmail.com.

References

1. P. Wang, V. M. Patel, and I. Hacihaliloglu, "Simultaneous segmentation and classification of bone surfaces from ultrasound using a multi-feature guided cnn," in *International Conference on Medical Image Computing and Computer-Assisted Intervention*, (Springer, 2018), 134-142.
2. D. Li, J. Wu, Y. He, X. Yao, W. Yuan, D. Chen, H.-C. Park, S. Yu, J. L. Prince, and X. D. Li, "Parallel deep neural networks for endoscopic OCT image segmentation," Biomedical Optics Express **10**, 1126-1135 (2019).
3. F. Liu, M. Hernandez-Cabronero, V. Sanchez, M. Marcellin, and A. Bilgin, "The current role of image compression standards in medical imaging," Information **8**, 131 (2017).
4. D. L. Donoho, "Compressed sensing," IEEE T Inform Theory **52**, 1289-1306 (2006).
5. A. M. Abdulghani and E. Rodriguez-Villegas, "Compressive sensing: From "Compressing while Sampling" to "Compressing and Securing while Sampling"," in *2010 Annual International Conference of the IEEE Engineering in Medicine and Biology*, 2010), 1127-1130.
6. Y. Blau and T. Michaeli, "The perception-distortion tradeoff," in *Proceedings of the IEEE Conference on Computer Vision and Pattern Recognition*, 2018), 6228-6237.
7. E. Agustsson, F. Mentzer, M. Tschannen, L. Cavigelli, R. Timofte, L. Benini, and L. V. Gool, "Soft-to-hard vector quantization for end-to-end learning compressible representations," in *Advances in Neural Information Processing Systems*, 2017), 1141-1151.
8. L. Theis, W. Shi, A. Cunningham, and F. Huszár, "Lossy image compression with compressive autoencoders," arXiv preprint arXiv:1703.00395 (2017).
9. S. J. Chiu, M. J. Allingham, P. S. Mettu, S. W. Cousins, J. A. Izatt, and S. Farsiu, "Kernel regression based segmentation of optical coherence tomography images with diabetic macular edema," Biomedical optics express **6**, 1172-1194 (2015).
10. K. Dabov, A. Foi, V. Katkovnik, and K. Egiazarian, "Image denoising by sparse 3-D transform-domain collaborative filtering. Image Processing, IEEE Transactions on 16 (8), pp. 2080-2095," (2007).
11. P. Wang, H. Zhang, and V. M. Patel, "SAR image despeckling using a convolutional neural network," IEEE Signal Processing Letters **24**, 1763-1767 (2017).
12. V. Iglovikov and A. Shvets, "Ternausnet: U-net with vgg11 encoder pre-trained on imagenet for image segmentation," arXiv preprint arXiv:1801.05746 (2018).
13. A. G. Roy, S. Conjeti, S. P. K. Karri, D. Sheet, A. Katouzian, C. Wachinger, and N. Navab, "ReLayNet: retinal layer and fluid segmentation of macular optical coherence tomography using fully convolutional networks," Biomedical optics express **8**, 3627-3642 (2017).

14. F. Milletari, N. Navab, and S.-A. Ahmadi, "V-net: Fully convolutional neural networks for volumetric medical image segmentation," in *2016 Fourth International Conference on 3D Vision (3DV)*, (IEEE, 2016), 565-571.
15. J. Johnson, A. Alahi, and L. Fei-Fei, "Perceptual losses for real-time style transfer and super-resolution," in *European conference on computer vision*, (Springer, 2016), 694-711.
16. Y. Han and J. C. Ye, "Framing U-Net via deep convolutional framelets: Application to sparse-view CT," IEEE transactions on medical imaging **37**, 1418-1429 (2018).
17. X. Wang and A. Gupta, "Generative image modeling using style and structure adversarial networks," in *European Conference on Computer Vision*, (Springer, 2016), 318-335.
18. D. Yoo, N. Kim, S. Park, A. S. Paek, and I. S. Kweon, "Pixel-level domain transfer," in *European Conference on Computer Vision*, (Springer, 2016), 517-532.
19. Y. Zhou and T. L. Berg, "Learning temporal transformations from time-lapse videos," in *European conference on computer vision*, (Springer, 2016), 262-277.
20. F. Mentzer, E. Agustsson, M. Tschannen, R. Timofte, and L. Van Gool, "Conditional probability models for deep image compression," in *Proceedings of the IEEE Conference on Computer Vision and Pattern Recognition*, 2018), 4394-4402.
21. P. Isola, J.-Y. Zhu, T. Zhou, and A. A. Efros, "Image-to-image translation with conditional adversarial networks," in *Proceedings of the IEEE conference on computer vision and pattern recognition*, 2017), 1125-1134.
22. Z. Wang, A. C. Bovik, H. R. Sheikh, and E. P. Simoncelli, "Image quality assessment: from error visibility to structural similarity," IEEE transactions on image processing **13**, 600-612 (2004).
23. A. Krizhevsky, I. Sutskever, and G. E. Hinton, "Imagenet classification with deep convolutional neural networks," in *Advances in neural information processing systems*, 2012), 1097-1105.
24. L. Bottou, "Stochastic gradient descent tricks," in *Neural networks: Tricks of the trade* (Springer, 2012), pp. 421-436.
25. Z. Wang, E. P. Simoncelli, and A. C. Bovik, "Multiscale structural similarity for image quality assessment," in *The Thrity-Seventh Asilomar Conference on Signals, Systems & Computers, 2003*, (IEEE, 2003), 1398-1402.
26. J. Oliveira, S. Pereira, L. Gonçalves, M. Ferreira, and C. A. Silva, "Multi-surface segmentation of OCT images with AMD using sparse high order potentials," Biomedical optics express **8**, 281-297 (2017).
27. O. Rippel and L. Bourdev, "Real-time adaptive image compression," in *Proceedings of the 34th International Conference on Machine Learning-Volume 70*, (JMLR. org, 2017), 2922-2930.
28. C. Ledig, L. Theis, F. Huszár, J. Caballero, A. Cunningham, A. Acosta, A. Aitken, A. Tejani, J. Totz, and Z. Wang, "Photo-realistic single image super-resolution using a generative adversarial network," in *Proceedings of the IEEE conference on computer vision and pattern recognition*, 2017), 4681-4690.
29. J. Pan, Y. Liu, J. Dong, J. Zhang, J. Ren, J. Tang, Y.-W. Tai, and M.-H. Yang, "Physics-based generative adversarial models for image restoration and beyond," arXiv preprint arXiv:1808.00605 (2018).
30. S. Ioffe and C. Szegedy, "Batch normalization: Accelerating deep network training by reducing internal covariate shift," arXiv preprint arXiv:1502.03167 (2015).
31. O. Ronneberger, P. Fischer, and T. Brox, "U-net: Convolutional networks for biomedical image segmentation," in *International Conference on Medical image computing and computer-assisted intervention*, (Springer, 2015), 234-241.
32. G. Toderici, D. Vincent, N. Johnston, S. Jin Hwang, D. Minnen, J. Shor, and M. Covell, "Full resolution image compression with recurrent neural networks," in *Proceedings of the IEEE Conference on Computer Vision and Pattern Recognition*, 2017), 5306-5314.
33. N. Johnston, D. Vincent, D. Minnen, M. Covell, S. Singh, T. Chinen, S. Jin Hwang, J. Shor, and G. Toderici, "Improved lossy image compression with priming and spatially adaptive bit rates for recurrent networks," in *Proceedings of the IEEE Conference on Computer Vision and Pattern Recognition*, 2018), 4385-4393.
34. J. Ballé, V. Laparra, and E. P. Simoncelli, "End-to-end optimized image compression," arXiv preprint arXiv:1611.01704 (2016).